

Transport evidence for the surface state and spin-phonon interaction in $\text{FeTe}_{0.5}\text{Se}_{0.5}$

Mu-Yun Li,^{1,2,*} Jia-Wei Hu,^{3,4,*} Ge Huang,¹ Wei-Jian Li,¹ Ya-Kang Peng,¹ Guangyong Xu,⁵ Genda Gu,⁶ and Xiao-Jia Chen^{1,7,†}

¹Center for High Pressure Science and Technology Advanced Research, Shanghai 201203, China

²Shanghai Institute of Space Power Source, Shanghai 200245, China

³Key Laboratory of Materials Physics, Institute of Solid State Physics, HFIPS, Chinese Academy of Sciences, Hefei 230031, China

⁴University of Science and Technology of China, Hefei 230026, China

⁵NIST Center for Neutron Research, National Institute of Standards and Technology, Gaithersburg, MD 20899, USA

⁶Condensed Matter Physics & Materials Science Division, Brookhaven National Laboratory, Upton, NY 11973, USA

⁷School of Science, Harbin Institute of Technology, Shenzhen 518055, China

(Dated: May 2, 2023)

The iron chalcogenides have been proved to be intrinsic topological superconductors to implement quantum computation because of their unique electronic structures. The topologically nontrivial surface states of $\text{FeTe}_{0.5}\text{Se}_{0.5}$ have been predicted by several calculations and then confirmed by high-resolution photoemission and scanning tunneling experiments. However, so far, the shreds of the electrical transport evidence for topological surface states are still in absence. By carrying out electrical transport experiments, we observe a topological transition with a nonlinear Hall conductivity and simultaneous linear magnetoresistance near the superconducting transition temperature. Furthermore, we observe a sign reversal of the Hall coefficient accompanied by a concurrently softening of the A_{1g} phonon mode at about 40 K, indicating a nematic transition. The synchronized phonon softening with nematicity manifests an enhanced fluctuation state through spin-phonon interaction. Our results solidly corroborate the topological surface states of $\text{FeTe}_{0.5}\text{Se}_{0.5}$ and provide an understanding of the mechanism of the superconductivity in iron chalcogenides.

I. INTRODUCTION

The iron chalcogenides are one of the most favored materials in the field of topological superconductivity¹ because of their structural simplicity², uncomplicated phase diagram³, and easily-substitution-tuned physical properties^{4,5}. The parent compound FeSe has a transition temperature (T_c) of 8 K under ambient pressure⁶, and of 37 K at a pressure of about 9 GPa⁷. Through proximity effect, a surprisingly higher T_c of 65 K was reported accompanied by a topological phase in the single-layer FeSe film on SrTiO_3 ⁸. It has been proposed that the lattice vibrations⁹ and excitations of electronic origin such as spin or electronic polarizability fluctuations⁶ are the two important candidates of Cooper pairing for high- T_c superconductivity in these superconductors. Later well-designed studies revealed that both are important to the pairing interaction strengths in FeSe¹⁰. The strong enhancement of T_c of the monolayer FeSe film was suggested to result from the strong electron-phonon coupling (EPC) played by an interface soft mode^{10–12}. Therefore, identifying the potential soft phonon modes in unconventional superconductors remains an arduous but necessary task and will help to understand the mechanism of superconductivity¹³. With increasing the concentration of the Te atom, an intense spin-orbit coupling effect is introduced in $\text{Fe}_{1+y}\text{Te}_x\text{Se}_{1-x}$ systems¹⁴ and the T_c rises to 14.5 K at x around 0.5¹⁵. The spin-orbit interaction will cause a band inversion near the Brillouin center. Thus, an s -wave superconducting gap on the surface state of $\text{FeTe}_{0.5}\text{Se}_{0.5}$ below T_c was observed by the recent

angle-resolved photoemission spectroscopy (ARPES) experiments, confirming the existence of the topological superconductivity^{15,16}. By tuning the nontrivial superconductivity on the surface, the iron chalcogenides can be a promising candidate for realizing Majorana bound states and paving the way for quantum computation^{17–19}.

The inverted electronic structure and spin-helical surface texture for $\text{FeTe}_{0.5}\text{Se}_{0.5}$ resemble those of topological insulators^{15,16,20}. As reported by Qu *et al.*, the acquired transport parameters of surface states can help to investigate the high-mobility Dirac fermions and Majorana bound states²¹. So far, there is little information on $\text{FeTe}_{0.5}\text{Se}_{0.5}$ in this aspect¹⁶. The lack of transport information on surface state, especially the carrier mobility, has hindered the further understanding of topological states in $\text{FeTe}_{0.5}\text{Se}_{0.5}$. Meanwhile, the mechanisms of unconventional superconductivity are still controversial issues^{6,9,10}. Previous Raman scattering experiments on iron chalcogenides were mainly focused on the lattice dynamics^{22–25}, while the features for superconductivity or other electronic states such as nematicity have not been reliably clarified. The systematical studies on the vibrational properties of high-quality single-crystal $\text{FeTe}_{0.5}\text{Se}_{0.5}$ are desirable. This could help the understanding of the mechanism(s) of superconductivity and the possible role of the electron-phonon coupling in iron-based superconductors.

In this work, we carry out the first-principles calculations, temperature-dependent electrical transport, and Raman scattering measurements to explore the topological superconductivity of single-crystal $\text{FeTe}_{0.5}\text{Se}_{0.5}$. We

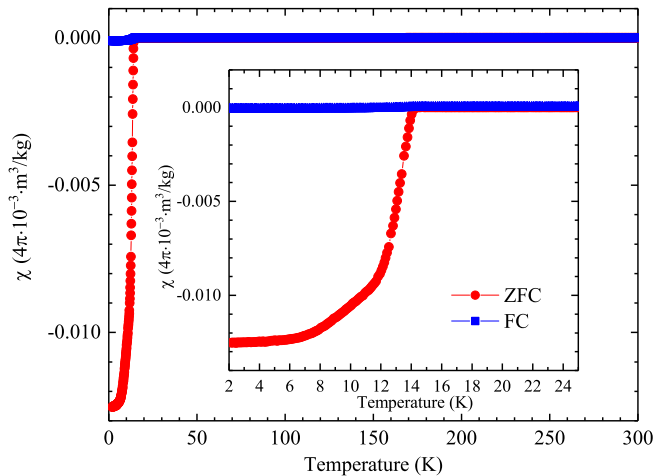


FIG. 1. Temperature dependence of the dc magnetization of $\text{FeTe}_{0.5}\text{Se}_{0.5}$. The magnetic fields were set to be 20 Oe. The red and blue symbols denote the data points of zero-field cooling (ZFC) and field cooling (FC), respectively. The inset demonstrates the magnification in the temperature range from 2 to 25 K. The T_c was determined to be 14.5 K for the studied sample.

corroborate a topological surface state with high mobility through transport measurements, which is consistent with our theoretical calculations. Combined with vibrational properties, we generally demonstrate the phase diagram of $\text{FeTe}_{0.5}\text{Se}_{0.5}$. We find a nematic transition followed by the appearance of the topological surface state. We conclude that both the spins and phonons play an essential role in the unconventional superconductivity of iron chalcogenides.

II. EXPERIMENTAL AND CALCULATION DETAILS

High-quality single crystal with nominal composition $\text{FeTe}_{0.5}\text{Se}_{0.5}$ was grown by the unidirectional solidification method. The oxygen-annealing method was used to remove the excess Fe atoms in the interstitial sites. The T_c of 14.5 K was determined by magnetization measurements with Quantum Design's Magnetic Properties Measurement System, as shown in Fig. 1. Fresh and clean surface of $\text{FeTe}_{0.5}\text{Se}_{0.5}$ was cleaved in the glove box for electrical transport and Raman scattering measurements with the size of about $150 \times 150 \mu\text{m}$ and the thickness of about $25 \mu\text{m}$.

The electrical resistivity (ρ) was measured with Quantum Design's Physical Property Measurement System using the standard four-probe method and Platinum electrodes. To eliminate the transverse (longitudinal) resistivity component from the misalignment of contacts, we obtained the ρ_{xy} and ρ_{xx} through $\rho_{xy} = [\rho_{xy}(+H) - \rho_{xy}(-H)]/2$ and $\rho_{xx} = [\rho_{xx}(+H) + \rho_{xx}(-H)]/2$, respectively. The components for the Hall conductivity along

the xx and xy directions are related to the two expressions $\sigma_{xx} = 1/\rho_{xx}$ and $\sigma_{xy} = \rho_{xy}/(\rho_{xx}^2 + \rho_{xy}^2)$.

The Raman spectra were collected using a single-stage spectrograph equipped with a thermoelectrically cooled charge-coupled device. The measurements were carried out on a freshly cleaved sample surface of the crystal using a laser with the wavelength of 488 nm in the temperature range from 296 to 5 K. The incident power was set below 1.5 mW with a spot diameter of about $10 \mu\text{m}$ to avoid the heating effect.

All the first-principles calculations were performed in the framework of the density functional theory^{26,27}, as implemented in the Vienna *ab initio* simulation package²⁸⁻³⁰. The spin-orbit coupling was included in the calculations. The Perdew-Burke-Ernzerhof of generalized gradient approximation was used for the exchange-correlation potential³¹. The optimized experimental lattice parameters³² were used to construct the crystal structure. The unit cell with nominal composition $\text{FeTe}_{0.5}\text{Se}_{0.5}$ was extended to a large one in the c direction, with two Fe atoms and one atom for each of the Te and Se elements involved (Fe_2TeSe). For both self-consistent field and non-self-consistent field calculations, a $9 \times 9 \times 6$ k -point mesh was used in the Brillouin zone, and the cut-off energy was set to 520 eV. The open-source software package (Wanniertools)³³ was used to investigate the topological nature on the projected (001) surface of $\text{FeTe}_{0.5}\text{Se}_{0.5}$. The s and p orbitals for Fe atoms and the p orbitals for Te/Se atoms were selected when employing the maximally localized Wannier functions³⁴.

III. RESULTS AND DISCUSSION

A. Dirac-cone-like surface state from calculations

The schematic structure of layered $\text{FeTe}_x\text{Se}_{1-x}$ with ordered Te/Se sites and the sketched Brillouin zone of $\text{FeTe}_{0.5}\text{Se}_{0.5}$ are presented in Fig. 2(a). Each of the Fe atoms is connected with four neighboring Te/Se atoms, forming a tetrahedron. Tuning the dopant level of Te/Se atoms introduces an enormous spin-orbit coupling effect and significantly influences the band structure near Fermi level (E_f)¹⁵. A topological transition emerges at around $x = 0.5$ ^{15,16}. The Brillouin zone of $\text{FeTe}_{0.5}\text{Se}_{0.5}$ has eight points with time-reversal symmetry which include $\Gamma(0,0,0)$, $M(\pi,\pi,0)$, $Z(0,0,\pi)$, $A(\pi,\pi,\pi)$, two $X(\pi,0,0)$, and two $R(\pi,0,\pi)$. The two-dimensional Brillouin zone of the (001) surface is projected along the k_z direction. Based on the k points of the Brillouin zone, Fig. 2(b) gives the calculated bulk electronic structure of $\text{FeTe}_{0.5}\text{Se}_{0.5}$. The band dispersion of the bulk state is generally consistent with the preceding theoretical predictions and ARPES experiments¹⁴⁻¹⁶. Previous studies substantiated the Dirac-cone-like surface states of $\text{FeTe}_{0.5}\text{Se}_{0.5}$ in the proximity to bulk superconductivity^{15,16}. Within the spin-orbit coupling, the nontrivial topological superconductivity is induced

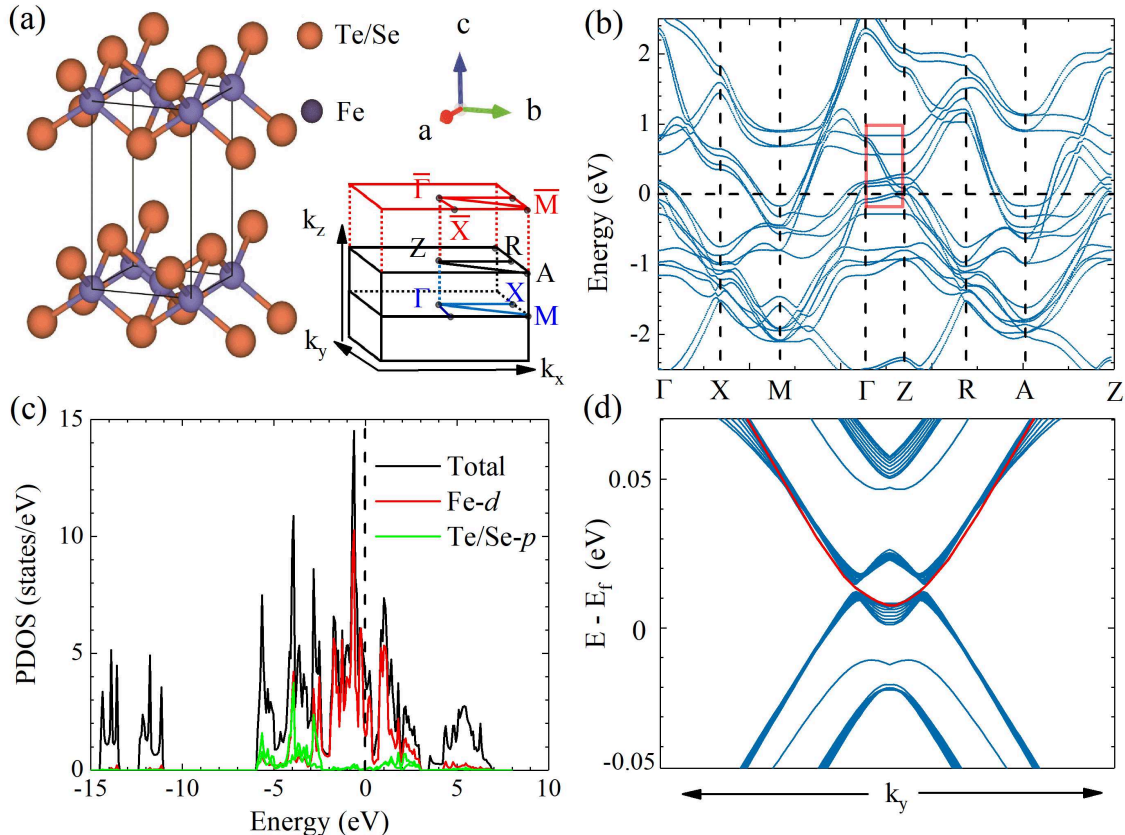


FIG. 2. (a) The schematic crystalline structure of Fe(Te,Se) and the sketch of the Brillouin zone of $\text{FeTe}_{0.5}\text{Se}_{0.5}$. The in-plane (001) surface Brillouin zone is projected along the k_z direction and marked by red solid lines. (b) Electronic band structure of $\text{FeTe}_{0.5}\text{Se}_{0.5}$. The red line marks the area where the band inversion emerges. (c) Electronic density of states of $\text{FeTe}_{0.5}\text{Se}_{0.5}$. The black solid line represents the total density of states. The red and green solid line denote the projected density of states of the Fe (d -orbit) and Te/Se (p -orbit) atoms, respectively. (d) Electronic band structure projected to the (001) surface. The red solid line shows the evident nontrivial Dirac-cone state.

by the band inversion between the Fe- d and Te/Se- p orbits along the Γ to Z direction. The place where the band inversion appears is marked by the red frame. For a better interpretation, Fig. 2(c) demonstrates the density of states for different atoms. The Fe- d and Te/Se- p orbits dominate the Fermi surface topology near E_f , although the weight of Te/Se- p components is relatively small. Based on the reliable bulk calculations, we constructed the tight-binding model to reveal the (001) surface's topological nature. Figure 2(d) displays the calculated Dirac-cone-like surface state along the k_y direction. An evident linear dispersion of the band structure near the E_f can be observed. The calculations demonstrate that the surface state is gapless and topologically nontrivial, consistent with previous reports^{15,16}. The linear dispersion of the electronic structure shares similarities with the surface-state band structures in topological insulators²¹. From the calculations, we conclude that $\text{FeTe}_{0.5}\text{Se}_{0.5}$ is a topological superconductor. The unique electronic structure indicates that when the neighboring bands are twisted into the Dirac cones, the carriers become high-mobility Dirac fermions. The results of the-

oretical calculations provide insightful guidance for the following experiments.

B. Electrical transport properties

Before carrying out the Hall effect measurements, it is necessary to examine the quality of the sample. Figure 3(a) presents the temperature dependence of the resistivity for $\text{FeTe}_{0.5}\text{Se}_{0.5}$. The inset displays the resistivities below 18 K at each applied magnetic field from 0 T to 9 T. The sample turns into a metallic state below 250 K ($d\rho/dT > 0$) and exhibits superconductivity at the temperature of about 15 K [See the magnetization measurements shown in the Fig. 1(a)]. With increasing magnetic field, the resistivity transition broadens and the T_c shifts to lower temperatures. Some similar broadening behaviors have been reported previously in other 11-type Fe-based systems³⁵. The relative high T_c value and metallic resistivity without the antiferromagnetic-like upturn illustrate that the crystal used is well annealed and that the distribution of excess Fe intersti-

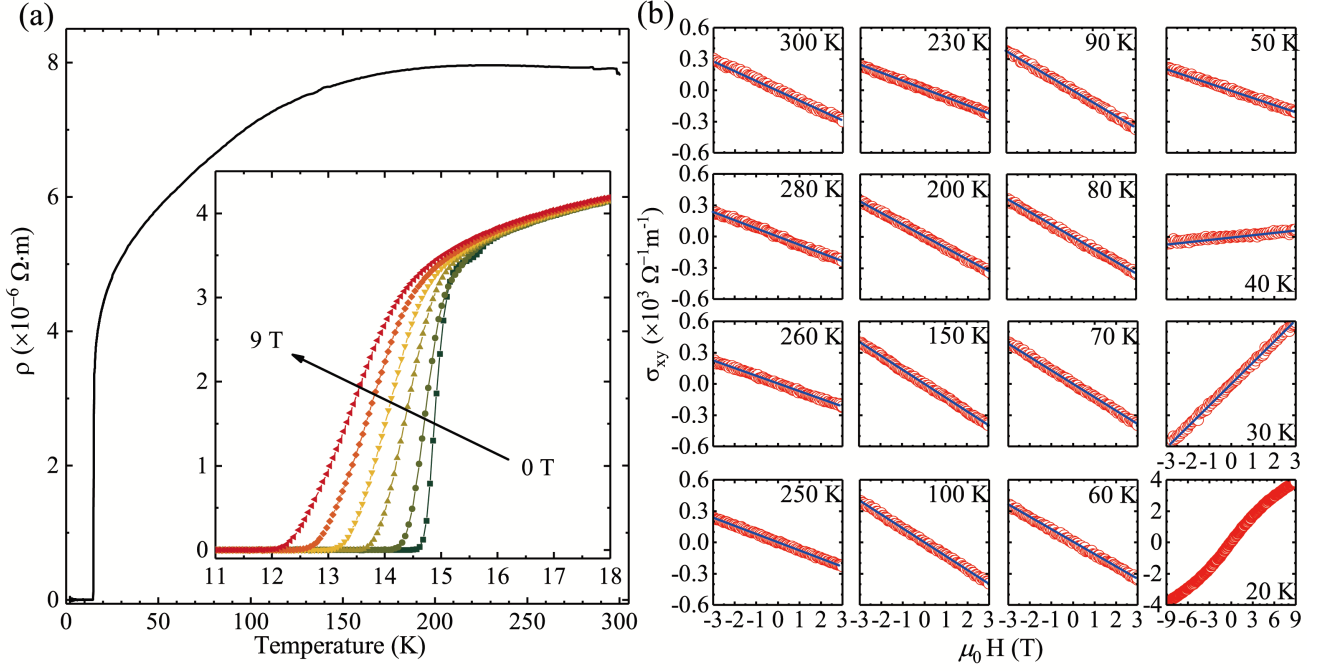


FIG. 3. (a) Temperature dependence of the electrical resistivity of $\text{FeTe}_{0.5}\text{Se}_{0.5}$ single crystal. The inset shows the temperature dependence of the resistivity at various magnetic fields up to 9 T. The applied field is parallel to the c axis. (b) Representative Hall conductivities of $\text{FeTe}_{0.5}\text{Se}_{0.5}$ at different temperatures. The red open circles and blue solid lines denote the experimental data points and linear fitting curves, respectively. The magnetic fields were set to change from -9 T to 9 T for a temperature of 20 K. At other temperatures, the magnetic fields were set to change from -3 T to 3 T.

tials can be ruled out^{36,37}. The excess Fe usually comes from inadequate O_2 -annealing and significantly affects the electronic properties. It could provide extra moments that localize the electrons^{38,39} and even cause a negative magnetoresistance³⁶. The excellent growth quality of our sample makes us confident for the following experiments and the related results.

For studying the topological properties of $\text{FeTe}_{0.5}\text{Se}_{0.5}$, we performed temperature-dependent Hall resistivity measurements. Figure 3(b) shows the Hall conductivity (σ_{xy}) at applied magnetic fields for some representative temperatures. The obtained Hall conductivity σ_{xy} follows a linear relationship with the applied magnetic field up to 3 T for temperatures from 300 K down to 30 K. Thus, the Hall coefficient (R_H) and carrier concentration (n_H) can be obtained from the single-band model⁴⁰:

$$R_H = \rho_{xy}/\mu_0 H \quad . \quad (1)$$

$$n_H = 1/eR_H \quad . \quad (2)$$

The slope ($d\sigma_{xy}/dH$) keeps negative above 50 K and becomes positive below 40 K, indicating that the dominant carriers change from the electrons to holes. The transport properties of dominant hole-like carriers at low temperature are similar to those reported by Pimentel *et al*⁴¹ but differ from others^{42,43}. In any case, as a common phenomenon in iron chalcogenides, the sign reversal of

R_H near 40 K can be explained by the Fermi surface reconstruction that leads to the nematic transition⁴⁴. In particular, numerous ARPES experiments reported the splitting of d_{xz}/d_{yz} bands near E_f , which triggers the structure evolution from the four-fold to two-fold symmetry^{43,45–47}.

When the temperature is lowered to 20 K, a distinctive nonlinear behavior is observed. Two features are noteworthy for the Hall conductivity at 20 K: Firstly, the σ_{xy} (or ρ_{xy}) deviates from linearity in the low field range, while in the normal state above 30 K, the linear behavior maintains up to 3 T. Secondly, the slope of the σ_{xy} - H curve remains positive up to 9 T, again confirming the dominant hole carriers in the low-temperature transport within the whole field range. For the topological insulating state, the Hall resistivity does not exhibit a linear behavior but has a resonant structure at the small magnetic field. The transport anomalies at 20 K are similar to those in other topological insulators, such as the Bi_2Te_3 and Bi_2Se_3 ^{21,48}, in which the surface states play a non-negligible role in the overall transport processes. Considering the recent ARPES results for $\text{FeTe}_{0.5}\text{Se}_{0.5}$ with a topological-insulator Dirac surface state at 15 K^{15,16}, we believe that the Hall and MR anomalies appearing in the vicinity of superconductivity are induced by the nontrivial electronic structure. Furthermore, a linear dependence of the magnetoresistance (MR) on the magnetic field appears coincidentally, as shown in Fig. 4(b),

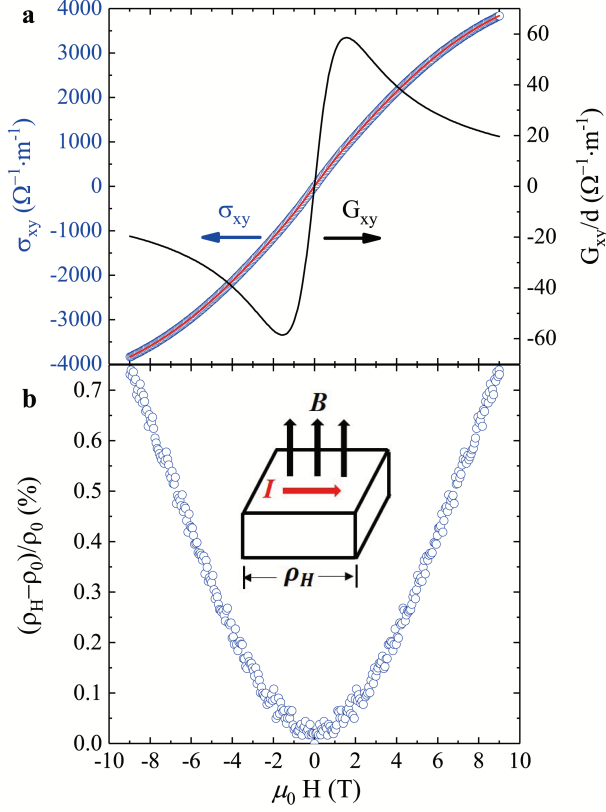


FIG. 4. (a) Magnetic field dependence of the Hall conductivity of $\text{FeTe}_{0.5}\text{Se}_{0.5}$ at the temperature of 20 K up to 9 T. The blue arrow pointing to the left axis denotes the whole conductivity (σ_{xy}). The black arrow pointing to the right axis represents the relevant surface term (G_{xy}). The blue circles denote the raw data points, with the red solid lines denoting the whole fitting results. (b) The magnetic-field-dependent magnetoresistance $[(\rho_H - \rho_0)/\rho_0]$ of $\text{FeTe}_{0.5}\text{Se}_{0.5}$ at the temperature of 20 K for the applied magnetic fields up to 9 T. The inset shows the schematic picture of measurements.

which can be interpreted as the result of the Dirac cone states^{16,48,49}. The results mentioned above offer an excellent opportunity for us to investigate the contributions of the surface state to the transport properties.

C. Transport evidence for the surface state

Figure 4 displays the Hall conductivity and MR at a temperature of 20 K as a function of the magnetic fields up to 9 T. The MR exhibits conventional parabolic line-shape at low magnetic fields. At higher fields, the MR increases linearly due to the quantum limit and corroborates the Dirac-cone-like band dispersion^{15,16,49}. The behavior of MR is a bit different in topological insulators, where the linear MR was also identified in the low magnetic field range^{21,50}. This is because the topological insulators have a much larger Landau level splitting

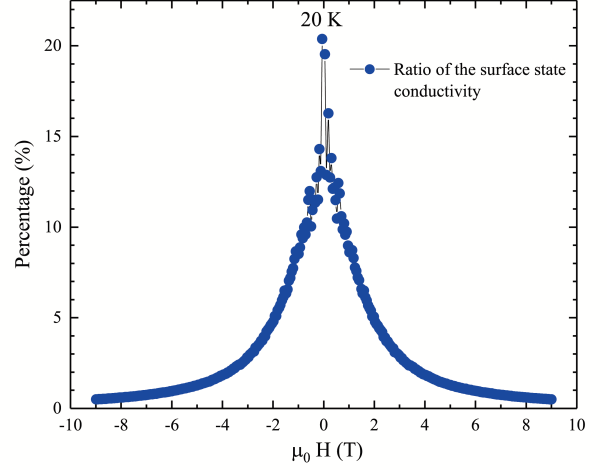


FIG. 5. The contribution of the surface state in $\text{FeTe}_{0.5}\text{Se}_{0.5}$ to the total conductivity at the magnetic field from -9 T to 9 T. The blue symbols denote the ratio of the surface state conductivity.

than the conventional bulk bands⁴⁹. Therefore, the quantum limit of topological insulators can be achieved in the lower magnetic field regions⁵¹. The MR of $\text{FeTe}_{0.5}\text{Se}_{0.5}$ at 9 T and 20 K (0.7%) is much larger than those of as-grown (0.03%) and half-annealed (0.14%) samples of $\text{Fe}_{1+y}\text{Te}_{0.6}\text{Se}_{0.4}$ ⁴⁹. The relatively large and positive MR again demonstrates the good growth quality of our sample³⁶. The observed Hall conductivity σ_{xy} can be described as the sum of the surface Hall conductivity σ_{xy}^s and the bulk σ_{xy}^b ²¹:

$$\sigma_{xy} = \sigma_{xy}^s + \sigma_{xy}^b \quad . \quad (3)$$

The surface conductivity σ_{xy}^s can be expressed as:

$$\sigma_{xy}^s = G_{xy}/d = \frac{2\pi e^3}{dh^2} \frac{Bl^2}{1 + (\mu_s B)^2} \quad . \quad (4)$$

Where B is the magnetic flux density, d is the sample thickness, l is the mean free path, and μ_s is the surface carrier mobility. The bulk conductivity σ_{xy}^b can be expressed by the semiclassical form:

$$\sigma_{xy}^b = p_{eff} e \mu_b \frac{\mu_b B}{1 + (\mu_b B)^2} \quad . \quad (5)$$

Where p_{eff} is the effective carrier concentration and μ_b is the bulk carrier mobility. The fitting matches well with the experimental data and gives $P_{eff} = 1.65 \times 10^{23} \text{ m}^{-3}$ and $l = 179 \text{ nm}$. The acquired value of the mean path for $\text{FeTe}_{0.5}\text{Se}_{0.5}$ is larger than that of FeSe (30 nm for the outer hole pocket β and 80 nm for the inner hole pocket δ in the Brillouin center)⁵², but close to that of Bi_2Se_3 (235 nm)²¹. Intriguingly, from Eqs. (3)-(5), the obtained mobility of the surface state ($6440 \text{ cm}^2\text{V}^{-1}\text{s}^{-1}$) is almost ten times larger than that of the bulk state ($610 \text{ cm}^2\text{V}^{-1}\text{s}^{-1}$).

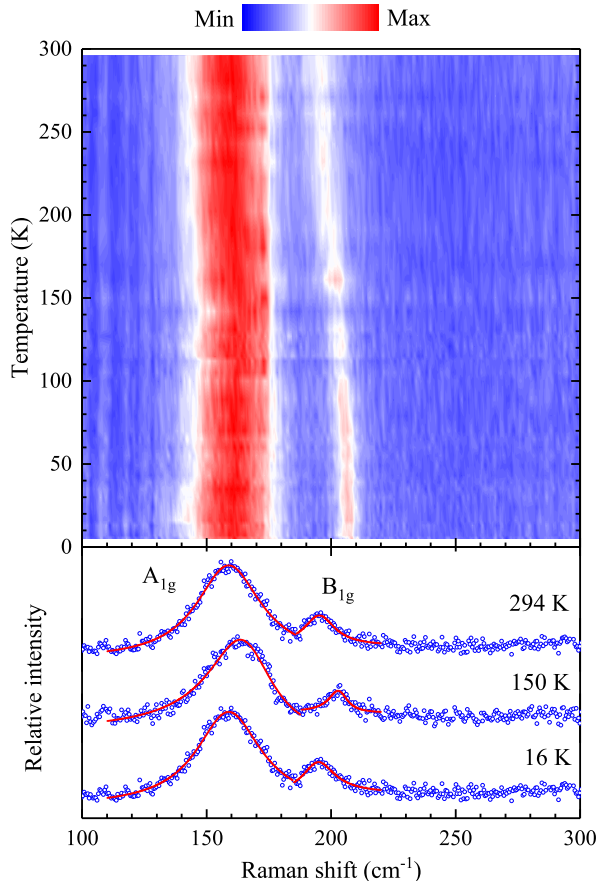


FIG. 6. (a) Mapping of the temperature-dependent Raman spectra of $\text{FeTe}_{0.5}\text{Se}_{0.5}$ from room temperature down to 4 K. The spectrum intensity denoted by different colors is presented at the top of the figure. The temperature evolution of the two phonon mode, the A_{1g} and B_{1g} mode, can be observed clearly. (b) Representative temperature-dependent Raman spectra of $\text{FeTe}_{0.5}\text{Se}_{0.5}$ at different temperatures. For clarity, three representative curves are displayed in this figure. The open circles and solid lines denote experimental data points and Fano fitting curves, respectively.

To be more specific, Fig. 5 shows the ratio of the surface state conductivity to the total conductivity ($\sigma_{xy}^s/\sigma_{xy}$). In the low magnetic field range, the surface state accounts for about 5% to a maximum of 20%. Despite the relatively small weight, the surface state can dominate the low-magnetic-field electrical transport with much higher mobility induced by the Dirac-cone-like band dispersion. The resonance Hall conductivity and nearly linear magnetoresistance have also been observed to serve as the evidence of nontrivial topological state in highly efficient thermoelectric materials^{55?}.

D. Phonon spectra in the superconducting and normal state

To further investigate the superconducting nature of $\text{FeTe}_{0.5}\text{Se}_{0.5}$, we systematically carried out the temperature-dependent Raman scattering measurements. The results are shown in Fig. 6. Two phonon modes, A_{1g} and B_{1g} , were observed in the temperature-dependent mapping of Fig. 6(a). The frequencies of the A_{1g} and B_{1g} phonon mode at room temperature are about 158 and 192 cm^{-1} , respectively. They are close to the earlier reported values^{25,53}. The linewidth of the A_{1g} mode is significantly larger than that of the B_{1g} mode. Both phonon modes show a hardening behavior with decreasing temperature. The hardening modes were commonly reported in $\text{FeTe}_x\text{Se}_{1-x}$ and were thought to be caused by the temperature-induced lattice contraction²⁵. Surprisingly, compared with the generally hardening trend, there apparently is a slight softening behavior of the A_{1g} mode below 40 K. This softening phonon mode will be analyzed and discussed in detail later. The representative Raman spectra at different temperatures are shown in Fig. 6(b). A marginally asymmetric phonon line shape emerges in the high-temperature range and becomes more notable at around 150 K. When the temperature decreases below 100 K, the symmetry of phonon peaks is profoundly refined. Taking this asymmetric effect into account, we used Fano function^{56,57} to fit the phonon spectra:

$$I(\omega) = I_0 \frac{\left(\frac{x-\omega_0}{\gamma} + q\right)^2}{1 + \left(\frac{x-\omega_0}{\gamma}\right)^2} + I_b(\omega) \quad (6)$$

Where ω_0 is the bare frequency, q is the parameter quantitatively characterizing asymmetry, γ is the phonon linewidth, I_0 is the parameter of intensity, and $I_b(\omega)$ denotes the background. The asymmetric lineshape turns back into Lorentzian lineshape when $q \rightarrow 0$. The Fano fitting matches well with our experimental data.

The detailed temperature evolution of the frequency and linewidth for the A_{1g} and B_{1g} mode using Fano fitting is shown in Fig. 7. Considering that the A_{1g} mode has a relatively small frequency change compared with its large phonon linewidth, we carefully designed and performed two-round Raman scattering experiments to ensure the consistency and accuracy of our results. We tried to measure the Raman spectra as detailed as possible in the low-temperature range which we most care about (4-50 K), with the temperature step less than 0.5 K. In the temperature range of 50-120 K, the temperature step was set to be about 1-3 K, while at higher temperatures this value was set to be around 5-10 K. The results of the first and second measurements match well with each other. Taking a brief look at the graph, we find a blueshift of the A_{1g} and B_{1g} mode when the temperature is decreased, as expected from the lattice contraction²⁵. The B_{1g} mode shows a larger hardening behavior than the A_{1g} mode, which can be attributed to the influence of the local

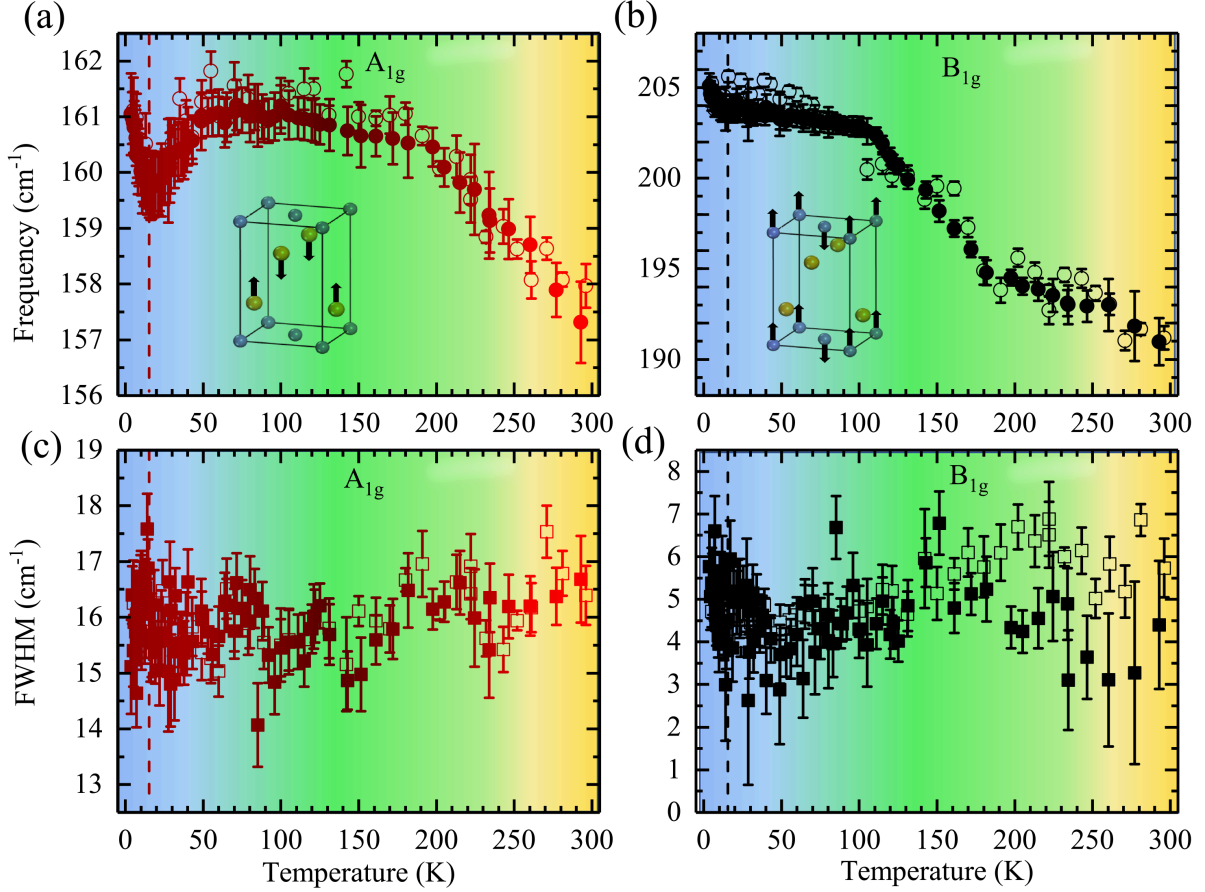


FIG. 7. (a)-(d) Temperature dependence of the phonon frequency and linewidth in FeTe_{0.5}Se_{0.5}. The crystal's point group symmetry probes the A_{1g} and B_{1g} channel. The inset graphs in (a) and (b) show the schematic illustrations for the A_{1g} and B_{1g} polarization mode. The blue atoms denote the Fe atoms, while the yellow atoms are the Te/Se atoms. The phonon frequency and linewidth of the A_{1g} and B_{1g} mode are displayed by the red and black symbols, respectively. The first and second rounds of the measurements are presented by the open and solid symbols, respectively. The four graphs are roughly divided into three parts using three different colors.

spin state of Fe atoms²⁴. Upon cooling, the linewidth of the B_{1g} mode generally narrows, with some abnormal changes showing up at around 250 and 40 K. The narrowing effect is well acknowledged because the linewidth is inversely proportional to the phonon lifetime^{58,59}. As the temperature cools down, the phonon lifetime increases, and the linewidth decreases. Yet, the narrowing of A_{1g} mode is almost undecipherable.

Nevertheless, the A_{1g} mode softens evidently at around 40 K, followed by the sign reversal of R_H mentioned above. We also used the Lorentzian function to fit the phonon lineshape, which turns out to have almost the same softening behavior below 40 K. Below T_c , the A_{1g} frequency rises again due to the self-energy effects⁶⁰. The sudden reduction of the A_{1g} phonon energy at 40 K, however, hasn't been reported previously in FeTe_{0.5}Se_{0.5} (or near $x = 0.5$) single crystals²⁵, probably because of the impurities or vacancies induced by imperfect growth conditions^{22,61}. Some similar softening anomalies have been found in FeTe²⁴ and the interface of the single-layer FeSe film on substrates¹¹. Notably, the great enhance-

ment of the T_c in thin FeSe film can be interpreted as the consequence of the enhanced EPC interaction^{11,12}. Moreover, previous calculations and ultra-fast dynamic experiments revealed that the A_{1g} mode is the most substantial phonon mode in the EPC spectra of iron chalcogenides^{62,63}. Correspondingly, it is not surprising to find the softening behavior of the A_{1g} mode in FeTe_{0.5}Se_{0.5}. Our results demonstrate the importance of the EPC on the superconductivity in iron chalcogenides.

E. Phase diagram for the superconducting, nematic, and normal state

To better illustrate the electronic and structural dynamics, we summarize the temperature-dependent Hall coefficient and carrier concentration obtained from Eqs. (1) and (2) in Fig. 8. The graph can be divided into three parts, denoted as three different colors like Fig. 7, to show a schematic phase diagram. The effective carrier concentration at 20 K is obtained by Equation (5)

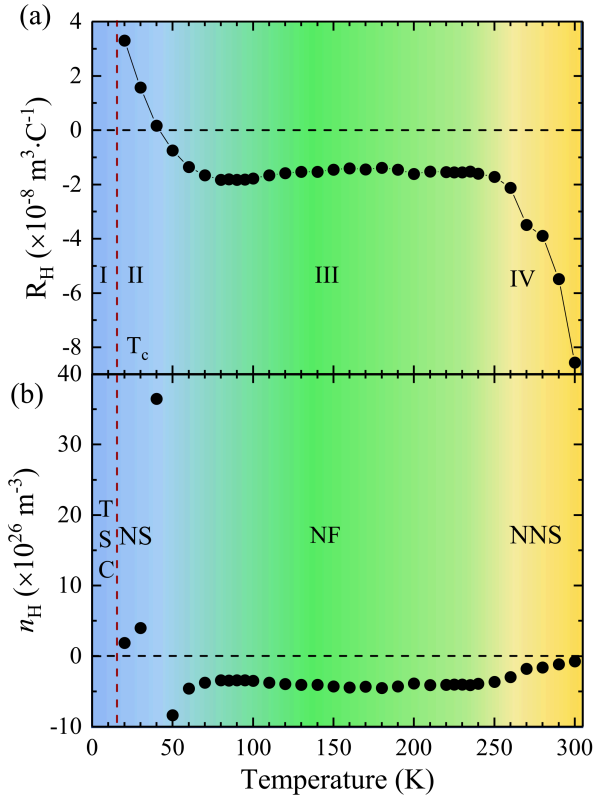


FIG. 8. Phase diagram of $\text{FeTe}_{0.5}\text{Se}_{0.5}$. Temperature dependence of the Hall coefficient (R_H) (a) and the effective carrier concentration (n_H) (b). The red dash line marks the T_c . The phase diagram can be divided into four parts using gradient ramp: (I) topological superconductivity (TSC), (II) nematic state (NS), (III) nematic fluctuations (NF), (IV) nonmetallic-normal state (NNS).

[$P_{eff}(20 \text{ K}) = 1.65 \times 10^{23} \text{ m}^{-3}$]. From 300 to 250 K (the yellow region IV), the sample shows a nonmetallic-normal state (NNS) for $d\rho/dT \leq 0$. The R_H changes drastically in this temperature range. Below 250 K (the green region III), a probable nematic fluctuations (NF) state is produced⁶³. At this time, the R_H and n_H suddenly turn to be almost constant. Simultaneously, an abnormality of the B_{1g} linewidth seems to appear. Below 40 K (the blue region I), the nematic state (NS) emerges due to the Fermi surface reconstruction. With further cooling (the blue region on the left side of the red dash line), topological superconductivity (TSC) is induced by the band inversion of Fe- $3d$ and Te/Se- p orbits near the hole pockets^{15,16}. The critical magnetic field measure for supporting the topological superconductivity in studied $\text{FeTe}_{0.5}\text{Se}_{0.5}$ was recently given by Yuan and Chen⁶⁴.

As seen from the schematic phase diagram, the topological superconductivity emerges right after the phonon softening and resides in the region of nematic order. It is natural to ask: what is the joint driving force behind these phenomena. The earlier widely accepted theory is

that the spin fluctuations give rise to both nematicity and superconductivity^{6,44}. However, the effect of phonons, especially the A_{1g} mode, cannot be simply omitted¹⁰⁻¹². In iron chalcogenides, the A_{1g} mode would induce huge fluctuations through spin-phonon coupling^{65,66}. The fluctuations-enhanced EPC can be accountable for the experimentally observed T_c of iron chalcogenides^{10,65}. That explains why the A_{1g} mode softens concomitantly with the nematic transition and becomes the softest at T_c . Our results provide a prospective approach to understanding the interrelationship between the spin fluctuations and EPC through transport and vibrational properties.

IV. CONCLUSIONS

In summary, we have found the nematic transition of $\text{FeTe}_{0.5}\text{Se}_{0.5}$ followed by the topological superconductivity with strong spin-phonon interaction from both the electrical transport and Raman scattering experiments. At around 250 K, a probable fluctuation state shows up with the explicit changes of the Hall coefficient, carrier concentration, and phonon linewidth. As the temperature is decreased to about 40 K, the compound undergoes a clear nematic transition, which is confirmed by the sign reversal of the Hall coefficient and the concurrent softening of the A_{1g} phonon mode. However, unlike other Se-doping rate samples such as $\text{FeTe}_x\text{Se}_{1-x}$, $\text{FeTe}_{0.5}\text{Se}_{0.5}$ does not exhibit an evident resistivity upturn at the nematic transition. That is probably due to the relatively small amplitude of nematicity compared with the extensive background. The softening A_{1g} mode at nematicity indicates a muscular spin-phonon interaction and an enhanced electron-phonon coupling strength in this superconductor. As the temperature is decreased down to 20 K, the nonlinear Hall conductivity and linear magnetoresistance are observed. Both corroborate the topological superconductivity on the surface. The high-mobility nontrivial topological surface state has been identified successfully from the bulk state through the anomalous transport properties. Our results shed light on understanding the multiple electronic phases and the spin-phonon interaction in iron-based superconductors.

V. ACKNOWLEDGEMENTS

This work was funded through the National Key R&D Program of China (Grant No. 2018YFA0305900) at HPSTAR, the Shenzhen Science and Technology Program (Grant No. KQTD20200820113045081), and the Basic Research Program of Shenzhen (Grant No. JCYJ20200109112810241). The work at BNL was supported by the US Department of Energy's the Office of Basic Energy Sciences with contract No. DOE-SC0012704.

- * These authors contributed equally to this work.
- † xjchen2@gmail.com
- ¹ G. Xu, B. Lian, P. Tang, X. L. Qi, and S. C. Zhang, Topological superconductivity on the surface of Fe-based superconductors, *Phys. Rev. Lett.* **117**, 047001 (2016).
 - ² R. Thomale, C. Platt, W. Hanke, J. P. Hu, and B. A. Bernevig, Exotic d -wave superconducting state of strongly hole-doped $K_xBa_{1-x}Fe_2As_2$, *Phys. Rev. Lett.* **107**, 117001 (2011).
 - ³ J. P. Sun, K. Matsuura, G. Z. Ye, Y. Mizukami, M. Shimozawa, K. Matsubayashi, M. Yamashita, T. Watashige, S. Kasahara, Y. Matsuda, J. Q. Yan, B. C. Sales, Y. Uwatoko, J. G. Cheng, and T. Shibauchi, Dome-shaped magnetic order competing with high-temperature superconductivity at high pressures in FeSe, *Nat. Commun.* **7**, 1 (2016).
 - ⁴ M. Abdel-Hafiez, Y. Y. Zhang, Z. Y. Cao, C. G. Duan, G. Karapetrov, V. M. Pudalov, V. A. Vlasenko, A. V. Sadakov, D. A. Knyazev, T. A. Romanova, D. A. Chareev, O. S. Volkova, A. N. Vasiliev, and X. J. Chen, Superconducting properties of sulfur-doped iron selenide, *Phys. Rev. B* **91**, 165109 (2015).
 - ⁵ K. Terao, T. Kashiwagi, T. Shizu, R. A. Klemm, and K. Kadowaki, Superconducting and tetragonal-to-orthorhombic transitions in single crystals of $FeSe_{1-x}Te_x$ ($0 \leq x \leq 0.61$), *Phys. Rev. B* **100**, 224516 (2019).
 - ⁶ T. Imai, K. Ahilan, F. L. Ning, T. M. McQueen, and R. J. Cava, Why does undoped FeSe become a high- T_c superconductor under pressure? *Phys. Rev. Lett.* **102**, 177005 (2009).
 - ⁷ S. Margadonna, Y. Takabayashi, Y. Ohishi, Y. Mizuguchi, Y. Takano, T. Kagayama, T. Nakagawa, M. Takata, and K. Prassides, Pressure evolution of the low-temperature crystal structure and bonding of the superconductor FeSe ($T_c = 37$ K), *Phys. Rev. B* **80**, 064506 (2009).
 - ⁸ N. N. Hao and J. P. Hu, Topological phases in the single-layer FeSe, *Phys. Rev. X* **4**, 031053 (2014).
 - ⁹ O. Rösch and O. Gunnarsson, Electron-phonon interaction in the t - J model, *Phys. Rev. Lett.* **92**, 146403 (2004).
 - ¹⁰ S. Gerber, S. L. Yang, D. Zhu, H. Soifer, J. A. Sobota, S. Rebec, J. J. Lee, T. Jia, B. Moritz, C. Jia, A. Gauthier, Y. Li, D. Leuenberger, Y. Zhang, L. Chaix, W. Li, H. Jang, J. S. Lee, M. Yi, G. L. Dakovski, S. Song, J. M. Glowia, S. Nelson, K. W. Kim, Y. D. Chuang, Z. Hussain, R. G. Moore, T. P. Devereaux, W. S. Lee, P. S. Kirchmann, and Z. X. Shen, Femtosecond electron-phonon lock-in by photoemission and x-ray free-electron laser, *Science* **357**, 71 (2017).
 - ¹¹ B. Rosenstein and B. Y. Shapiro, High-temperature superconductivity in single unit cell layer FeSe due to soft phonons in the interface layer of the SrTiO₃ substrate, *Phys. Rev. B* **100**, 054514 (2019).
 - ¹² J. J. Lee, F. T. Schmitt, R. G. Moore, S. Johnston, Y. T. Cui, W. Li, M. Yi, Z. K. Liu, M. Hashimoto, Y. Zhang, D. H. Lu, T. P. Devereaux, D. H. Lee, and Z. X. Shen, Interfacial mode coupling as the origin of the enhancement of T_c in FeSe films on SrTiO₃, *Nature* **515**, 245 (2014).
 - ¹³ X. J. Chen, Exploring high-temperature superconductivity in hard matter close to structural instability, *Matter Radiat. Extremes* **5**, 068102 (2020).
 - ¹⁴ Z. J. Wang, P. Zhang, G. Xu, L. K. Zeng, H. Miao, X. Y. Xu, T. Qian, H. M. Weng, P. Richard, A. V. Fedorov, H. Ding, X. Dai, and Z. Fang, Topological nature of the FeSe_{0.5}Te_{0.5} superconductor, *Phys. Rev. B* **92**, 115119 (2015).
 - ¹⁵ P. Zhang, K. Yaji, T. Hashimoto, Y. Ota, T. Kondo, K. Okazaki, Z. J. Wang, J. S. Wen, G. D. Gu, H. Ding, and S. Shin, Observation of topological superconductivity on the surface of an iron-based superconductor, *Science* **360**, 182 (2018).
 - ¹⁶ P. Zhang, Z. J. Wang, X. X. Wu, K. Yaji, Y. Ishida, Y. Kohama, G. Y. Dai, Y. Sun, C. Bareille, K. Kuroda, K. Okazaki, K. Kindo, X. C. Wang, C. Q. Jin, J. P. Hu, R. Thomale, K. Sumida, S. L. Wu, K. Miyamoto, T. Okuda, H. Ding, G. D. Gu, T. Tamegai, T. Kawakami, M. Sato, and S. Shin, Multiple topological states in iron-based superconductors, *Nat. Phys.* **15**, 41 (2019).
 - ¹⁷ C. Nayak, S. H. Simon, A. Stern, M. Freedman, and S. Das Sarma, Non-Abelian anyons and topological quantum computation, *Rev. Mod. Phys.* **80**, 1083 (2008).
 - ¹⁸ D. F. Wang, L. Y. Kong, P. Fan, H. Chen, S. Y. Zhu, W. Y. Liu, L. Cao, Y. J. Sun, S. X. Du, J. Schneeloch, R. D. Zhong, G. D. Gu, L. Fu, H. Ding, and H. J. Gao, Evidence for Majorana bound states in an iron-based superconductor, *Science* **362**, 333 (2018).
 - ¹⁹ T. Machida, Y. Sun, S. Pyon, S. Takeda, Y. Kohsaka, T. Hanaguri, T. Sasagawa, and T. Tamegai, Zero-energy vortex bound state in the superconducting topological surface state of Fe(Se,Te), *Nat. Mater.* **18**, 811 (2019).
 - ²⁰ O. V. Yazyev, J. E. Moore, and S. G. Louie, Spin polarization and transport of surface states in the topological insulators Bi₂Se₃ and Bi₂Te₃ from first principles, *Phys. Rev. Lett.* **105**, 266806 (2010).
 - ²¹ D. X. Qu, Y. S. Hor, J. Xiong, R. J. Cava, and N. P. Ong, Quantum oscillations and Hall anomaly of surface states in the topological insulator Bi₂Te₃, *Science* **329**, 821 (2010).
 - ²² T. L. Xia, D. Hou, S. C. Zhao, A. M. Zhang, G. F. Chen, J. L. Luo, N. L. Wang, J. H. Wei, Z. Y. Lu, and Q. M. Zhang, Raman phonons of α -FeTe and Fe_{1.03}Se_{0.3}Te_{0.7} single crystals, *Phys. Rev. B* **79**, 140510 (2009).
 - ²³ K. Okazaki, S. Sugai, S. Niitaka, and H. Takagi, Phonon, two-magnon, and electronic Raman scattering of Fe_{1+y}Te_{1-x}Se_x, *Phys. Rev. B* **83**, 035103 (2011).
 - ²⁴ V. Gnezdilov, Y. Pashkevich, P. Lemmens, A. Gusev, K. Lamonova, T. Shevtsova, I. Vitebskiy, O. Afanasiev, S. Gnatchenko, V. Tsurkan, J. Deisenhofer, and A. Loidl, Anomalous optical phonons in FeTe chalcogenides: Spin state, magnetic order, and lattice anharmonicity, *Phys. Rev. B* **83**, 245127 (2011).
 - ²⁵ Y. J. Um, A. Subedi, P. Toulemonde, A. Y. Ganin, L. Boeri, M. Rahlenbeck, Y. Liu, C. T. Lin, S. J. E. Carlsson, A. Sulpice, M. J. Rosseinsky, B. Keimer, and M. Le Tacon, Anomalous dependence of c -axis polarized Fe B_{1g} phonon mode with Fe and Se concentrations in Fe_{1+y}Te_{1-x}Se_x, *Phys. Rev. B* **85**, 064519 (2012).
 - ²⁶ P. Hohenberg and W. Kohn, Inhomogeneous electron gas, *Phys. Rev.* **136**, 864 (1964).
 - ²⁷ W. Kohn and L. J. Sham, Self-consistent equations including exchange and correlation effects, *Phys. Rev. A* **140**, 1133 (1965).

- ²⁸ G. Kresse and J. Hafner, Ab initio molecular dynamics for liquid metals, *Phys. Rev. B* **47**, 558 (1993).
- ²⁹ G. Kresse and J. Hafner, Ab initio molecular-dynamics simulation of the liquid-metal amorphous-semiconductor transition in germanium, *Phys. Rev. B* **49**, 14251 (1994).
- ³⁰ G. Kresse and J. Furthmüller, Efficient iterative schemes for ab initio total-energy calculations using a plane-wave basis set, *Phys. Rev. B* **54**, 11169 (1996).
- ³¹ J. P. Perdew, K. Burke, and M. Ernzerhof, Generalized gradient approximation made simple, *Phys. Rev. Lett.* **77**, 3865 (1996).
- ³² S. L. Li, C. de la Cruz, Q. Huang, Y. Chen, J. W. Lynn, J. P. Hu, Y. L. Huang, F. C. Hsu, K. W. Yeh, M. K. Wu, and P. C. Dai, First-order magnetic and structural phase transitions in $\text{Fe}_{1+y}\text{Se}_x\text{Te}_{1-x}$, *Phys. Rev. B* **79**, 054503 (2009).
- ³³ Q. S. Wu, S. N. Zhang, H. F. Song, M. Troyer, and A. A. Soluyanov, WannierTools: An open-source software package for novel topological materials, *Comput. Phys. Commun.* **224**, 405 (2018).
- ³⁴ I. Souza, N. Marzari, and D. Vanderbilt, Maximally localized Wannier functions for entangled energy bands, *Phys. Rev. B* **65**, 035109 (2001).
- ³⁵ H. C. Lei, R. W. Hu, E. S. Choi, J. B. Warren, and C. Petrovic, Pauli-limited upper critical field of $\text{Fe}_{1+y}\text{Te}_{1-x}\text{Se}_x$, *Phys. Rev. B* **81**, 094518 (2010).
- ³⁶ J. Hu, T. J. Liu, B. Qian, and Z. Q. Mao, Coupling of electronic and magnetic properties in $\text{Fe}_{1+y}(\text{Te}_{1-x}\text{Se}_x)$, *Phys. Rev. B* **88**, 094505 (2013).
- ³⁷ Y. Sun, Y. Tsuchiya, T. Taen, T. Yamada, S. Pyon, A. Sugimoto, T. Ekino, Z. X. Shi, and T. Tamegai, Dynamics and mechanism of oxygen annealing in $\text{Fe}_{1+y}\text{Te}_{0.6}\text{Se}_{0.4}$ single crystal, *Sci. Rep.* **4**, 4585 (2014).
- ³⁸ T. J. Liu, X. Ke, B. Qian, J. Hu, D. Fobes, E. K. Vehstedt, H. Pham, J. H. Yang, M. H. Fang, L. Spinu, P. Schiffer, Y. Liu, Z. Q. Mao, and J. P. Hu, Charge-carrier localization induced by excess Fe in the superconductor $\text{Fe}_{1+y}\text{Te}_{1-x}\text{Se}_x$, *Phys. Rev. B* **80**, 174509 (2009).
- ³⁹ Y. Sun, T. Taen, Y. Tsuchiya, Q. Q. Ding, S. S. Pyon, Z. X. Shi, and T. Tamegai, Large, homogeneous, and isotropic critical current density in oxygen-annealed $\text{Fe}_{1+y}\text{Te}_{0.6}\text{Se}_{0.4}$ single crystal, *Appl. Phys. Express.* **6**, 043101 (2013).
- ⁴⁰ T. Otsuka, S. Hagiwara, Y. Koshika, S. Adachi, T. Usui, N. Sasaki, S. Sasaki, S. Yamaguchi, Y. Nakanishi, M. Yoshizawa, S. Kimura, and T. Watanabe, Incoherent-coherent crossover and the pseudogap in Te-annealed superconducting $\text{Fe}_{1+y}\text{Te}_{1-x}\text{Se}_x$ revealed by magnetotransport measurements, *Phys. Rev. B* **99**, 184505 (2019).
- ⁴¹ J. L. Pimentel, P. Pureur, M. A. Vila, and R. A. Ribeiro, Magnetotransport properties and Seebeck effect in the superconductor $\text{FeSe}_{0.5}\text{Te}_{0.5}$, *J. Phys.: Conf. Ser.* **480**, 012016 (2014).
- ⁴² C. S. Zhu, J. H. Cui, B. Lei, N. Z. Wang, C. Shang, F. B. Meng, L. K. Ma, X. G. Luo, T. Wu, Z. Sun, and X. H. Chen, Tuning electronic properties of $\text{FeSe}_{0.5}\text{Te}_{0.5}$ thin flakes using a solid ion conductor field-effect transistor, *Phys. Rev. B* **95**, 174513 (2017).
- ⁴³ G. C. Lin, J. Guo, Y. L. Zhu, S. Cai, Y. Z. Zhou, C. Huang, C. L. Yang, S. J. Long, Q. Wu, Z. Q. Mao, T. Xiang, and L. L. Sun, Correlation between Fermi surface reconstruction and superconductivity in pressurized $\text{FeTe}_{0.55}\text{Se}_{0.45}$, *Phys. Rev. B* **101**, 214525 (2020).
- ⁴⁴ Q. S. Wang, Y. Shen, B. Y. Pan, Y. Q. Hao, M. W. Ma, F. Zhou, P. Steffens, K. Schmalzl, T. R. Forrest, M. Abdel-Hafez, X. J. Chen, D. A. Chareev, A. N. Vasiliev, P. Bourges, Y. Sidis, H. B. Cao, and J. Zhao, Strong interplay between stripe spin fluctuations, nematicity and superconductivity in FeSe, *Nat. Mater.* **15**, 159 (2016).
- ⁴⁵ T. Shimojima, S. Y. uzuki, T. Sonobe, A. Nakamura, M. Sakano, J. Omachi, K. Yoshioka, M. Kuwata-Gonokami, K. Ono, H. Kumigashira, A. E. Böhmer, F. Hardy, T. Wolf, C. Meingast, H. V. Löhneysen, H. Ikeda, and K. Ishizaka, Lifting of xz/yz orbital degeneracy at the structural transition in detwinned FeSe, *Phys. Rev. B* **90**, 121111 (2014).
- ⁴⁶ K. Nakayama, Y. Miyata, G. N. Phan, T. Sato, Y. Tanabe, T. Urata, K. Tanigaki, and T. Takahashi, Reconstruction of band structure induced by electronic nematicity in an FeSe superconductor, *Phys. Rev. Lett.* **113**, 237001 (2014).
- ⁴⁷ P. Zhang, T. Qian, P. Richard, X. P. Wang, H. Miao, B. Q. Lv, B. B. Fu, T. Wolf, C. Meingast, X. X. Wu, Z. Q. Wang, J. P. Hu, and H. Ding, Observation of two distinct d_{xz}/d_{yz} band splittings in FeSe, *Phys. Rev. B* **91**, 214503 (2015).
- ⁴⁸ X. L. Wang, Y. Du, S. X. Dou, and C. Zhang, Room temperature giant and linear magnetoresistance in topological insulator Bi_2Te_3 nanosheets, *Phys. Rev. Lett.* **108**, 266806 (2012).
- ⁴⁹ Y. Sun, T. Taen, T. Yamada, S. S. Pyon, T. Nishizaki, Z. X. Shi, and T. Tamegai, Multiband effects and possible Dirac fermions in $\text{Fe}_{1+y}\text{Te}_{0.6}\text{Se}_{0.4}$, *Phys. Rev. B* **89**, 144512 (2014).
- ⁵⁰ A. A. Taskin, Z. Ren, S. Sasaki, K. Segawa, and Y. Ando, Observation of Dirac holes and electrons in a topological insulator, *Phys. Rev. Lett.* **107**, 016801 (2011).
- ⁵¹ A. A. Abrikosov, Quantum magnetoresistance, *Phys. Rev. B* **58**, 2788 (1998).
- ⁵² T. Terashima, N. Kikugawa, A. Kiswandhi, E. S. Choi, J. S. Brooks, S. Kasahara, T. Watashige, H. Ikeda, T. Shibauchi, Y. Matsuda, T. Wolf, A. E. Böhmer, F. Hardy, C. Meingast, H. V. Löhneysen, M. T. Suzuki, R. Arita, S. and Uji, Anomalous Fermi surface in FeSe seen by Shubnikov-de Haas oscillation measurements, *Phys. Rev. B* **90**, 144517 (2014).
- ⁵³ C. Camerlingo, E. Bellingeri, C. Nappi, E. Sarnelli, and C. Ferdeghini, Raman investigation of Fe-based chalcogenide films, *Physica B* **586**, 411966 (2020).
- ⁵⁴ L. C. Chen, P. Q. Chen, W. J. Li, Q. Zhang, V. V. Struzhkin, A. F. Goncharov, Z. F. Ren, and X. J. Chen, Enhancement of thermoelectric performance across the topological phase transition in dense lead selenide, *Nat. Mater.* **18**, 1321 (2019).
- ⁵⁵ H. J. Pang, H. Yu, Wei-Jian Li, L. C. Chen, P. F. Qiu, Q. Peng, and X. J. Chen, Topological states of thermoelectric Yb-filled skutterudites, *Phys. Rev. B* **107**, 125202 (2023).
- ⁵⁶ A. M. Zhang and Q. M. Zhang, Electron-phonon coupling in cuprate and iron-based superconductors revealed by Raman scattering, *Chin. Phys. B.* **22**, 087103 (2013).
- ⁵⁷ K. C. Hewitt, X. K. Chen, C. Roch, J. Chrzanowski, J. C. Irwin, E. H. Altendorf, R. Liang, D. Bonn, and W. N. Hardy, Hole concentration and phonon renormalization of the 340-cm^{-1} B_{1g} mode in 2% Ca-doped $\text{YBa}_2\text{Cu}_3\text{O}_y$ ($6.76 < y < 7.00$), *Phys. Rev. B* **69**, 064514 (2004).
- ⁵⁸ P. G. Klemens, Anharmonic decay of optical phonons, *Phys. Rev.* **148**, 845 (1996).
- ⁵⁹ J. Menéndez and M. Cardona, Temperature dependence of the first-order Raman scattering by phonons in Si, Ge, and $\alpha\text{-Sn}$: Anharmonic effects, *Phys. Rev. B* **29**, 2051 (1984).

- ⁶⁰ S. F. Wu, A. Almoalem, I. Feldman, A. Lee, A. Kanigel, and G. Blumberg, Superconductivity and phonon self-energy effects in $\text{Fe}_{1+y}\text{Te}_{0.6}\text{Se}_{0.4}$, *Phys. Rev. Research* **2**, 013373 (2020).
- ⁶¹ C. S. Lopes, C. E. Foerster, F. C. Serbena, P. R. Júnior, A. R. Jurelo, J. L. P. Júnior, P. Pureur, and A. L. Chinelatto, Raman spectroscopy of highly oriented $\text{FeSe}_{0.5}\text{Te}_{0.5}$ superconductor, *Supercond. Sci. Technol.* **25**, 025014 (2012).
- ⁶² A. Subedi, L. J. Zhang, D. J. Singh, and M. H. Du, Density functional study of FeS, FeSe, and FeTe: Electronic structure, magnetism, phonons, and superconductivity, *Phys. Rev. B* **78**, 134514 (2008).
- ⁶³ C. W. Luo, I. H. Wu, P. C. Cheng, J. Y. Lin, K. H. Wu, T. M. Uen, J. Y. Juang, T. Kobayashi, D. A. Chareev, O. S. Volkova, and A. N. Vasiliev, Quasiparticle dynamics and phonon softening in FeSe superconductors, *Phys. Rev. Lett.* **108**, 257006 (2012).
- ⁶⁴ N. F. Q. Yuan and X. J. Chen, Critical field measure for topological superconductivity, arXiv: 2209.00816.
- ⁶⁵ Q. Q. Ye, K. Liu, and Z. Y. Lu, Influence of spin-phonon coupling on antiferromagnetic spin fluctuations in FeSe under pressure: First-principles calculations with van der Waals corrections, *Phys. Rev. B* **88**, 205130 (2013).
- ⁶⁶ S. Mandal, R. E. Cohen, and K. Haule, Strong pressure-dependent electron-phonon coupling in FeSe, *Phys. Rev. B* **89**, 220502 (2014).